




RESEARCH ARTICLE | SEPTEMBER 09 2025

X-ray crystal spectrometer throughput, data treatment, and configuration over the JET DTE2 and DTE3 campaigns

A. M. Patel ; N. C. Hawkes ; K.-D. Zastrow; M. O'Mullane ; JET Contributors;
The EUROfusion Tokamak Exploitation Team



Rev. Sci. Instrum. 96, 093503 (2025)

<https://doi.org/10.1063/5.0274324>



View
Online



Export
Citation

Articles You May Be Interested In

Estimating the neutron yield in a deuterium–tritium plasma with the JET neutron camera

Rev. Sci. Instrum. (June 2025)

ICRH operations and experiments during the JET-ILW tritium and DTE2 campaigns

AIP Conf. Proc. (August 2023)

ICRH options for JET-ILW DTE2 operation

AIP Conf. Proc. (September 2020)



MCL
MAD CITY LABS INC.

Closed Loop Nanopositioning Systems with Picometer precision, Low noise and High stability

Force Microscopy and Single Molecule Microscopy Instruments for Quantum, Materials, and Bioscience

Custom Design and Innovative Solutions for the Nanoscale World

Think Nano® | Positioning | Microscopy | Solutions




X-ray crystal spectrometer throughput, data treatment, and configuration over the JET DTE2 and DTE3 campaigns

Cite as: Rev. Sci. Instrum. 96, 093503 (2025); doi: 10.1063/5.0274324

Submitted: 5 April 2025 • Accepted: 22 August 2025 •

Published Online: 9 September 2025



A. M. Patel,^{1,a)} N. C. Hawkes,¹ K.-D. Zastrow,¹ M. O'Mullane,² JET Contributors^{b)}
and The EUROfusion Tokamak Exploitation Team^{c)}

AFFILIATIONS

¹United Kingdom Atomic Energy Authority, Culham Campus, Abingdon, Oxfordshire OX14 3DB, United Kingdom

²Department of Physics, University of Strathclyde, Glasgow, G1 1XJ, United Kingdom

^{a)}Author to whom correspondence should be addressed: ash.patel@ukaeea.uk

^{b)}See author list of: "Overview of T and D-T results in JET with ITER-like wall" by Maggi *et al.* Nucl. Fusion **64**, 112012 (2023).

^{c)}See author list of: "Overview of the EUROfusion Tokamak Exploitation program in support of ITER and DEMO" by Joffrin *et al.* Nucl. Fusion **64**, 112019 (2024).

ABSTRACT

The calibration of the JET x-ray spectrometer is presented. The absolute throughput, diffractor focusing, and instrument function of the spectrometer are presented, and the quality of the ion temperature measurement is re-assessed, particularly at the lower end. The addition of a second diffractor enables the simultaneous measurements of the spectra from H- and He-like nickel, which widens the spatial coverage of the core-ion temperature measurements for high-performance plasmas at a fixed Bragg angle range. A calculation of the absolute continua from the spectrum background from the second diffractor is analyzed for different JET plasmas. The spectrometer's narrow bandwidth makes it ideal as an "x-ray monochromator" that can sample a single energy channel (or two over the two crystal orders) within the free-free and free-bound x-ray continua. The measurable effect for impurity-seeded plasmas is explored as a means to determine the plasma concentration of the seeding impurities, which has the potential to be a robust method for high performance DT operations in reactor-class machines.

© 2025 Author(s). All article content, except where otherwise noted, is licensed under a Creative Commons Attribution-NonCommercial-NoDerivs 4.0 International (CC BY-NC-ND) license (<https://creativecommons.org/licenses/by-nc-nd/4.0/>). <https://doi.org/10.1063/5.0274324>

INTRODUCTION

The JET facility¹ is a tokamak plasma where the ion temperatures have exceeded 10 keV over the core region during deuterium–tritium operations in the DTE2 and DTE3 campaigns.^{2,3} Resonance line emission from H- and He-like ions of the intrinsic impurity nickel occurs in the 1–2 Å wavelength region, and these spectra are rich in satellite lines on the long wavelength side of the resonance lines.^{4,5} Doppler-broadened line profiles and absolute intensities, along with high-resolution spectral measurements, are an important way to evaluate local electron temperatures, impurity ion temperatures, and their concentrations, as well as an ionization equilibrium determination.⁶

The x-ray spectrometer deployed in JET since the inception⁷ is in the Johann configuration⁸ with a large Rowland circle diameter, resulting in ~20 m long beam lines converging onto a crystal-diffraction chamber box. The optical axis, at the center of the field of view, is tangential to the inner vacuum-vessel wall as shown in the general layout in Fig. 1. The principal advantages of a very large diameter include negligible optical aberrations of the cylindrically bent diffractor, good wavelength resolution, and the ability to separate the detector from noise and damage by isolating the sensor from the plasma both by distance and by locating it behind the biological shield-wall. The Si/Ge diffractor damage over JET campaigns is negligible due to its location and low neutron dose.⁹ However, for reactor-class machines, a planar pre-disperser that has a high

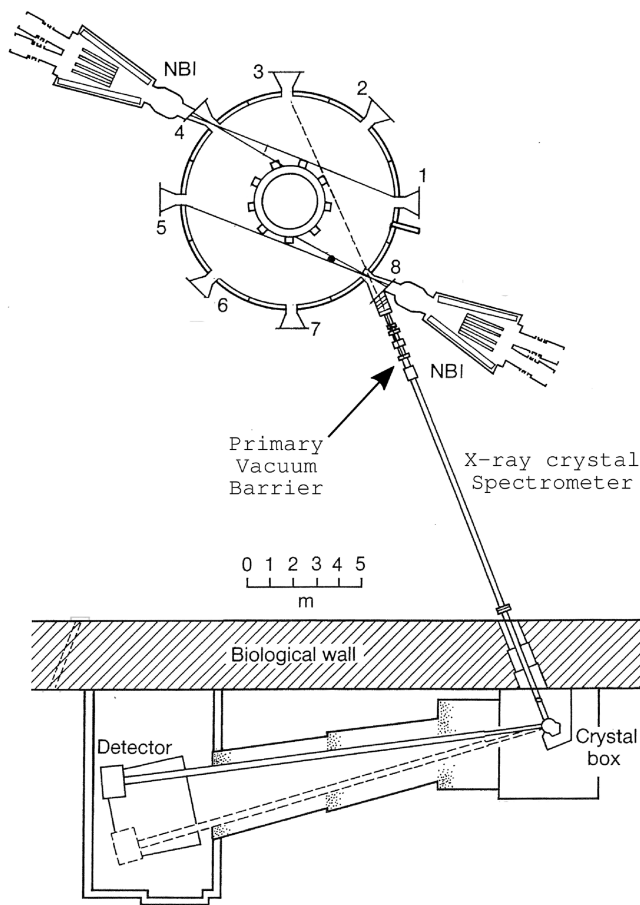


FIG. 1. Layout of the high-resolution x-ray crystal spectrometer at the JET facility. Neutral beam injection (NBI) systems are also shown.

threshold, e.g., for neutron damage, will be required to deflect the required x-ray energies to crystal spectrometers.¹⁰ Further details on upgrades to the original spectrometer, including the introduction of a second parallel, independent spectrometer system; large-area three-stage gas electron multiplier sensors; new data acquisition systems; a high-definition diffractor; and arm motion control, are summarized in Ref. 11.

The profile of the emission from a spectral line of an ion is determined by the electron temperature and density profiles and by cross field impurity transport and plasma rotation. For emission arising in the core region, i.e., $r/a < 0.6$, the latter effects are small, and ionization equilibrium between ion stages may be assumed. The ionization potentials of Ni^{25+} , Ni^{26+} , and Ni^{27+} (Li-, He-, and H-like Ni) are 2.4, 10.3, and 10.7 keV, respectively, leading to a wide He-like Ni profile for most JET discharges, which have central electron temperatures in the 2–5 keV range. H-like ions are only seen in higher performance and higher central electron temperature plasmas. The JET x-ray spectrometer measures line-integrated and background emissivity along the line of sight, so any localization must be modeled.

This paper is organized into sections detailing the instrument, its configuration, tolerances, and sensitivity, with a section on interpreting the line and continuum emission in hydrogenic, helium, and impurity-seeded plasmas. Absolute continua analysis, as detailed here, may complement other quantitative measurements in existing and future reactor-class machines such as ITER,¹² where diagnostics are challenged with plasma-facing optics degradation from material deposition and damage due to neutron irradiation^{13,14} and will have to be limited or mitigated with design considerations.¹⁵

Instrument detail

The two spectrometers are parallel and stacked vertically, inclined such that the respective optical axes from the sensor and crystal meet at a small angle at the center of the primary vacuum barrier (see Fig. 1). This consists of a beryllium foil supported by a grid structure—at the Rowland circle—which is capable of withstanding a pressure differential of up to an atmosphere and separates the torus vacuum from the spectrometer vacuum, which is normally maintained at $\sim 10^{-4}$ mbar.

Table I details the wavelength ranges and diffractor integrated reflectivities, R_c , for the Ge and Si crystal-based spectrometers. Using the He-like spectral feature, comprising the “w” resonance line at 1.5884 Å and satellite lines, to measure ion temperatures is the primary purpose of the instrument, and data are available for the majority of JET discharges. The H-like Ni-Ly_{α_1} (1.5303 Å) is measured by the new Si diffractor. The measured emission will at most be 20% of the He-like “w” resonance line from the Ge crystal assuming similar spatial emission profiles—here, the 41% drop in the Si diffractor reflectivity is compounded with the fact that light from only a single plasma-pass is made due to vignetting; hence, the signal to noise levels will be poorer for the H-like stage (see the sections titled Absolute Throughput and Vignetting). However, fitting the line shape, including accounting for the satellite lines’ contribution, gives a good measure of the ion temperature averaged over the spatial profile of the respective ion stages. These effectively independent spectrometer systems, which extend the ion temperature range but also have some overlap, are the motivation for adding the Si diffractor.

Pulse-height (energy-resolved) sensor data for both spectrometers are shown in Fig. 2. Spectra that contain the H- and He-like Ni emissions are isolated at the second order; He-like signals are

TABLE I. Sensor wavelength ranges covered with the installed Si and Ge diffractors at a Bragg angle of $\sim 52.67^\circ$ at 1.5884 Å. H- and He-like Ni Ly_{α_1} and “w” lines are of primary interest for ion-temperature. R_c is the diffractor integrated reflectivity.

Crystal	Order	$2d$ (Å)	λ_{\min} (Å)	λ_{\max} (Å)	R_c (μrad)	$R_c/(R_c \text{ Ge440})$
Si	1	3.840 312	3.042	3.066	56	2.6
	2		1.521	1.533	8.9	0.41
	3		1.014	1.022	1.8	0.08
Ge	1	3.995 4	3.170	3.194	134	6.3
	2		1.585	1.597	21.4	$\equiv 1$
	3		1.057	1.065	4.37	0.20

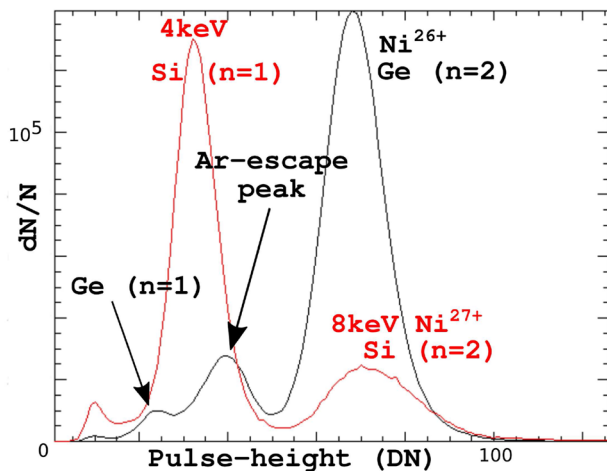


FIG. 2. Typical pulse-height distributions from the two spectrometers (JET No. 99 360)—both Ni emissions are selected from the second order spectra. Si diffractor data are shown in red. Mylar attenuators are used to reduce the first orders such that the overall count rates are comfortably within sensor saturation limits. The $n = 3$ signals are negligible.

especially strong, which leads to good ion temperature estimates from line-fitting as well as being well time-resolved. This short wavelength part of the spectra with the highest signal levels is the “main-stay” of the system. The Ge diffractor, a spectral bandpass, encompasses the He-like Ni spectra in the 1.585–1.597 Å wavelength region.

The remainder of this section will outline the methods for the laboratory focusing of both diffractors prior to the DTE2 and DTE3 campaigns, vignetting at the center of the field of view, and instrument throughput.

Diffractor bend quality

The large focal length places the diffractors and sensors outside the torus hall. The radius of curvature of the crystal laminae is ~ 25 m, which places strict requirements on the quality of the material and on the accuracy when preparing the diffractor.¹⁶ The crystal dimensions are $230 \times 35 \times 5$ mm³, and they are cut parallel to the 220 plane for both the Ge and Si plates. As discussed in Ref. 16, focusing the crystal in visible light is transferable to the x-ray domain, so no other procedure is required to quantify the contribution of diffractor curvature defects to the total instrumental resolution.

The double crystal bending jig, developed specifically on site for JET, consists of two vertically separated four pillar systems utilizing multiple micrometers to cylindrically bend the crystals with relative tilt and rotation control. This assembly, with kinematic positioning, is mounted magnetically within the vacuum box. The whole assembly can be moved to the laboratory for the bending process, which is now described.

The crystal is clamped near each edge by stainless steel pillars (top photo in Fig. 3: “Active area”); the front ones are fixed, with the outer rear pair being pushed against the back of the crystal surface by means of a series of micrometers for each diffractor. Special attention had to be paid to ensure the stability of the curvature over

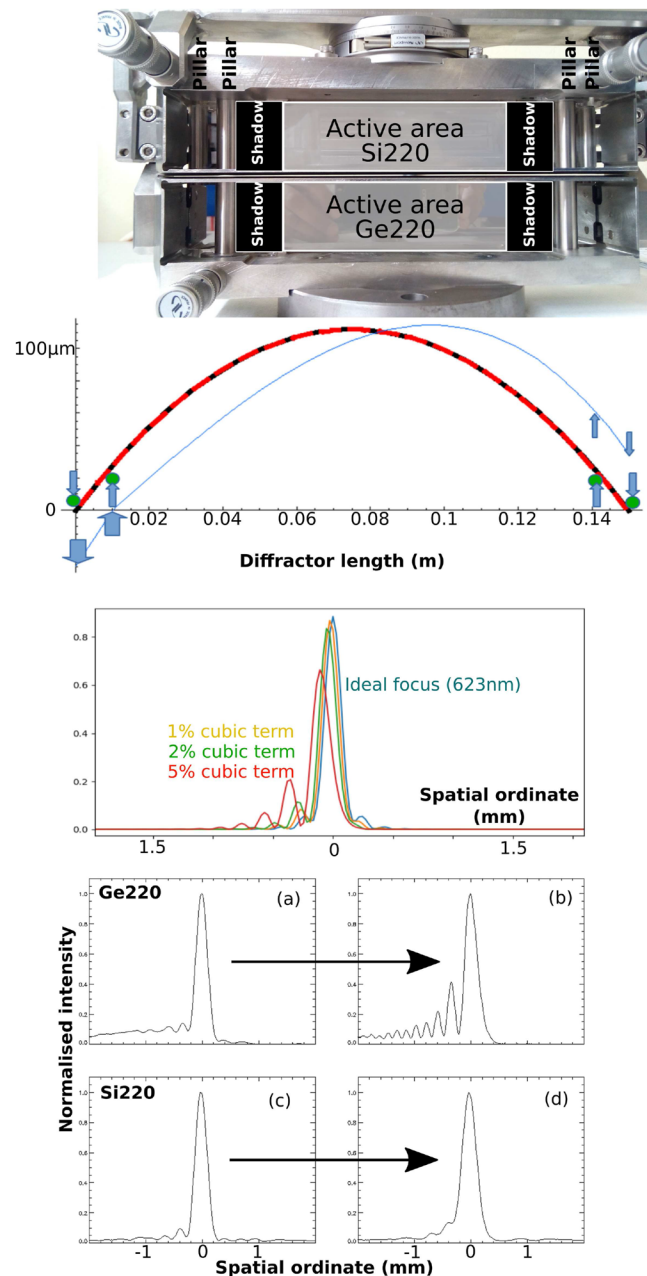


FIG. 3. Diffractor bending jig (top photo)—front pillars can be seen with the x-ray active area clearly shown. The next two figures show the cylindrically bent focus quality model with a distortion introduced due to asymmetrical pillar movement leading to off-axis structure(s). Actual measurements of Ge and Si spectrometers before (a) and (c) and after (b) and (d) the move to the vacuum box are measured in-lab. The Si crystal mechanism is consistently more stable over the move/pump-down procedure.

time. Shifts of ~ 0.1 m of the focal position usually occur within 12 h after the bend exercise. Small excursions also occur during transport to the vacuum chamber, pump-down, and the re-measuring procedure of the focus quality (instrument function) and position—most

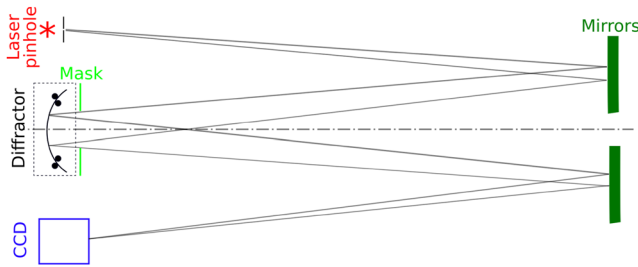


FIG. 4. Layout diagram illustrating how the laser, pinhole, mirrors, bending jig, and a 2D area sensor are arranged during the diffractor-bending procedure. The distance between the pinhole/diffractor-surface/sensor and mirror surfaces is half the Rowland circle diameter. The mask width defines the active diffractor area that is illuminated by the x rays at the Bragg angle under consideration—taking into account the shadows cast by the pillars.

probably due to thermal excursions and vibrations during kinematic clamping of the jig.

For these exercises, a red solid-state laser with small divergence is used behind a $100\ \mu\text{m}$ pinhole to ensure that the active area of the crystal is painted (see Fig. 4), i.e., is uniformly illuminated by the central region of the Airy disk. A large-area 2D CCD sensor is placed at the focus of the crystal, giving a real-time image measurement. The diffractors are locally masked such that only the areas illuminated by x rays during operation are exposed (top photo in Fig. 3: “Active area”). The resulting image for the Si crystal assembly is stable when comparing measurements from before and after the jig was transported to/from the kinematic mount in the crystal box and the laboratory. The mechanism was left alone after the best focus was achieved. The measurement of the diffraction pattern is in qualitative agreement with ray-tracing calculations, also shown in Fig. 3, where the point spread function is calculated using a ray-tracing program from an ideal cylinder (quadratic) with different levels of (cubic) distortions introduced, e.g., from non-symmetrical

small movement of the pillar(s). The blue curve in Fig. 3 represents the distorted crystal shape (e.g., if one of the four pillars did not press on the crystal at all), here represented with a cubic polynomial term, a percentage of which is added to the ideal (red curve) shape. Different levels of cubic distortions added to the ideal focus change the point-spread function, as illustrated in the third panel.

Low ion temperature assessment

Measurements show that the new Si diffractor has better bend stability than the mainstay Ge one. However, this can be used advantageously to determine an upper limit of the Ge instrument function by using emission from the JET plasma itself. Lowest density, radio frequency (RF) heated plasmas have high electron temperatures but low ion temperatures due to the electron-ion equipartition timescales. In such plasmas, there is strong emission from both H- and He-like ions of nickel, but the Doppler width compared with the instrument function width will be the smallest.

In Figs. 5(a) and 5(b), we show the He-like and H-like Ni spectra from the two spectrometers. Also shown are the partial fits to the main “w” and the Ly_{α_1} lines and satellites and the instrument functions used in the fit.

As usual, the ion temperatures are deduced from the Gaussian component of the fit. Figure 5(c) illustrates how the He-like Ni ion temperatures so calculated could vary as the instrument function component width is varied over the fits to the data. In this plasma pulse, as He-like ion temperatures cannot exceed the H-like, an effective upper-limit to the Ge220 instrument function width is obtained.

The instrument function will be of less significance for standard plasmas, where ion temperatures are substantially higher and where the Doppler component dominates.

The ion temperature is thus extracted from the line of sight measurement by fitting the spectrum to an emission model and the measured instrument function. A local equilibrium balance between

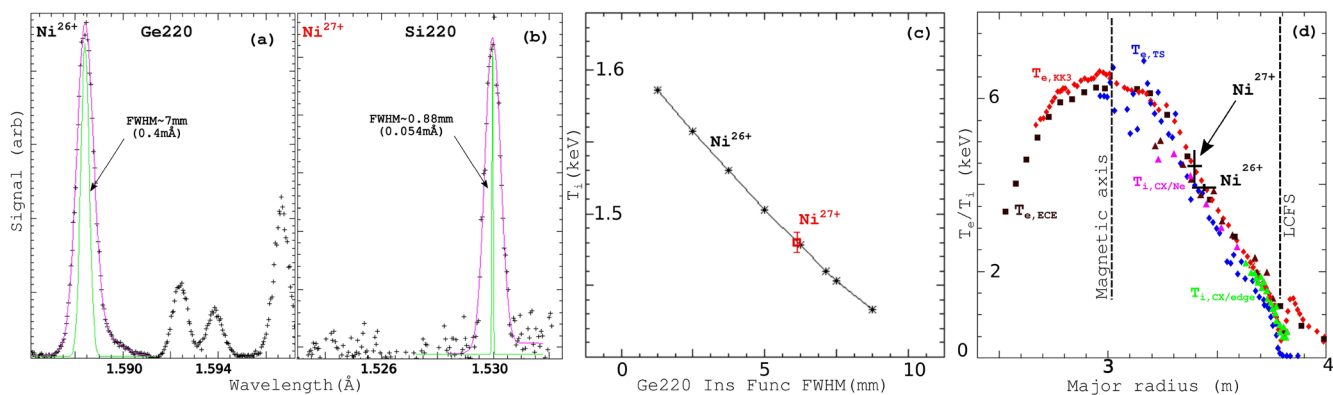


FIG. 5. [(a) and (b)] Ge220 and Si220 spectra (JET No. 105 613, 11.4–17.4 s), respectively, and partial fits (in magenta) to the main resonant emission and satellites—using the upper-limit of the instrument function (green) for the Ge220 spectrometer. (c) Calculated $\text{Ni}^{26+} T_i$ from the Doppler component as the Ge220 instrument width is varied—an upper limit of $\sim 7\ \text{mm}$ is set by the Ni $\text{Ly}_{\alpha_1} T_i$, which has a robust instrument function, and (d) for most JET plasmas the Doppler-width dominates: here, we compare ion temperatures from the spectrometers with other measurements (JET No. 105 781, 12.5 s). T_e is from Thomson scattering (TS) and electron cyclotron emission (ECE, KK3); the other T_i are from charge-exchange (CX) systems.

the H- and He-like nickel ions is assumed, using measured electron temperature and density profiles. The atomic data for ionization and recombination rates are from ADAS,¹⁷ and relative satellite-line intensities follow those of Ref. 18. In Fig. 5(d), the ion temperatures for H- and He-like Ni are shown with their spatial ordinate being the centroid and a single standard deviation calculated from the fit. The figure highlights the fact that the H- and He-like Ni ion temperatures are in good agreement with other measurement techniques and, for this plasma, with measured electron temperatures.

Vignetting

As noted here and in Refs. 11 and 16, the He-like Ni²⁶⁺ emission is firmly at the center of the Ge220 spectrometer double-pass view range and does not suffer from any vignetting. However, the field of view for the Ni-Ly_{α1} line does partly span the inner wall boundary area (see Fig. 1). From suitable plasma temperature and density conditions, it is possible to select data frames that exclude any line emission across the field of view. An effective vignetting function may then be estimated by analyzing continua over many pulses and applied to higher performance plasmas when the line emission is present. The experimentally generated vignetting curve is shown in Fig. 6(a), where the Impact Parameter, IP, is the distance between the tangent of the sensor/pixel line-of-sight to the machine axis,

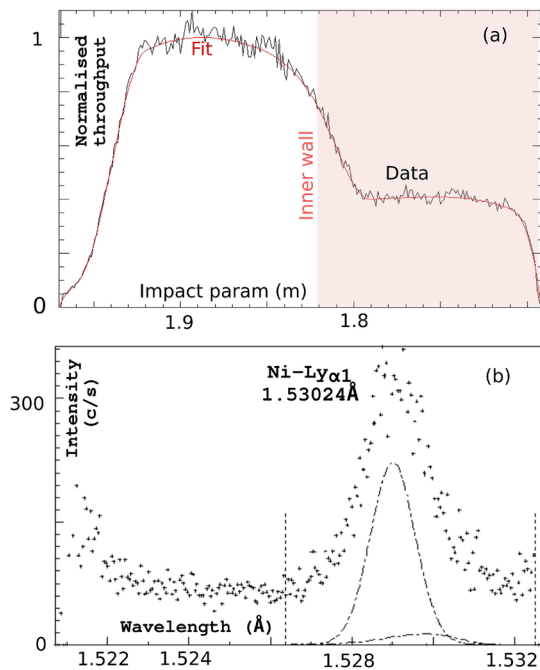


FIG. 6. (a) Vignetting over the center of the field of view from continua with data frames that are carefully selected to exclude line radiation—namely, lower core temperature plasmas where Ni-Ly_{α1} intensities are negligible. (b) Example application to the H-like Ni-Ly_{α1} and associated satellites for JET pulse No. 105 775, over the time period 7.7–7.9 s. The emissivity peak and standard deviation at $r/a = 0.3 \pm 0.09$, $T_i \approx 6.74 \pm 0.6$ keV, and $T_e = 7.96 \pm 2.94$ keV (T_e from TS ~ 8 keV for this r/a region). The impact parameter (IP) axis shown in (a) is mapped to the wavelength scale in (b).

$$IP = R_0 \sin(\theta_0 - \theta_B) \sim C - n\lambda/2d, \quad (1)$$

where n , $2d$, θ_B , λ , R_0 , θ_0 , and C are the diffraction order, lattice-spacing, Bragg angle (subtended by sensor/pixel to the diffractor surface), wavelength, and various constants from the JET-spectrometer geometry, respectively. The rollover at the edges of the crystal is due to the line of sight obstructions. The fit to a spectrum with a prominent Ni-Ly_{α1} and satellites, from a high performance, high electron temperature plasma, is shown in Fig. 6(b). The main emission and satellite lines fitted show the importance of accounting for the vignetting.

Spectrometer sensitivity

The sensitivity for a Johann x-ray spectrometer geometry may be expressed as $S = LT\eta$, where T is the system transmission, η is the detector efficiency, and the luminosity is given by $L = R_c A h_d / 2R$, which is a function of the diffractor reflectivity (R_c), crystal area (A), sensor height (h_d), and the Rowland circle radius (R).

A schematic layout of the spectrometer is given in Fig. 7, showing all the components from the barrier at the JET plasma to the sensor. The optical throughput is the same for both spectrometers apart from the diffractors, an air gap difference due to the relative sensor positions, and the Mylar attenuators. These are used to attenuate the brighter first order emission to a level similar to that of the second order so that the sensor may operate optimally below its saturation limit. The alignment of the centers of the sensors, diffractors, and barriers is achieved using low-divergence visible lasers, and the alignment of the spectrometer, both in air and under vacuum, has been historically robust. One of the more difficult measurements to make is the transmission fraction of the Mylar attenuators. This is naturally low, and because of insufficiently accurate tolerances in the manufacturing process, it is necessary to measure this value on a continuous basis by monitoring an *in situ* ⁵⁵Fe source over the active areas of the sensors. Attenuation at the principal 5.9 keV energy is measured, and the lower energy

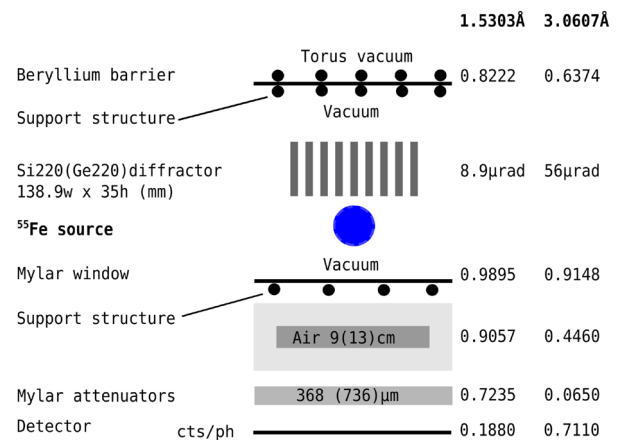


FIG. 7. Schematic of all spectrometer attenuation components. Fractional attenuation at the two energies over the first and the second diffraction orders for the Si crystal is also printed. Values in brackets are for the Ge220 spectrometer. The ⁵⁵Fe source is located in the vacuum and paints all components from that position to the sensors. Diffractor integrated reflectivities (in μrad) are listed at each energy.

value is derived from the properties of Mylar given in the CXRO database (URL: https://henke.lbl.gov/optical_constants/). The sensor efficiency components, for 5 and 12 μm Mylar with 0.2 μm Al and a 15 mm conversion gap operating with a detector gas mixture of 70:30% ArCO_2 , have been characterized in detail¹⁹ at the operation energies in question, values of which are also shown in Fig. 7 for the Si diffractor spectrometer.

ABSOLUTE THROUGHPUT

For most JET plasmas, the He-like lines of nickel cover the Ge spectrometer sensor's width in both the first and second orders. In contrast, the H-like Ly_{α_i} line observed by the Si spectrometer is only significant during high-temperature plasmas (>5 keV). Furthermore, only one $\text{Ar}16^+$ line (≈ 3.056 Å, $1s^2-1s8p^{20}$) is present in the spectrum during argon-seeded plasmas. Therefore, the Si spectrometer is mostly line-free and is ideal for the study of continua.

Continuum emission from the hydrogen (and its isotopes) fuel and impurities is due to bremsstrahlung (free-free) and radiative recombination (free-bound) processes. The absolute levels of the continuum, over the small wavelength bandpass of the instrument (Table I), may be calculated using the measured instrument sensitivity outlined in the previous section. Atomic data for the model are from ADAS²⁹ with modeled continuum emission following the methods of Ref. 21. The calculations use the measured profiles of the electron temperature and density from the high resolution Thomson scattering diagnostic, and the mapping from flux-surfaces to chordal line of sight (EFIT²²) is needed to evaluate the integrated line of sight predictions.

A strong check on the viability of this method is to consider the special cases where the plasma effective charge $Z_{\text{eff}} = 1$, for helium plasmas where $Z_{\text{eff}} = 2$, and in seeded argon plasmas where argon emission is significant. In these plasmas, the continuum emission can be calculated. Z_{eff} calculated from the Si spectrometer in first order and second order, namely, over 3.042–3.066 Å (~ 4 keV) and 1.521–1.533 Å (~ 8 keV) with a shorthand nomenclature of 4/8 keV, may be compared to the independent measurement based on emission in the visible part of the spectrum, here termed VB (Z_{eff} measurements from VB are detailed in Ref. 23).

“Clean” plasmas

The time evolution of the VB (Z_{eff}) measurement compared to that measured and modeled (based on measured density, temperature, and line-of-sight flux structure) at the 4 and 8 keV energies for a JET pulse is shown in Fig. 8. The error bar in the time dimension is due to sufficient counting statistics, and that of the intensity is a single standard deviation from the fit over that time interval.

Over the steady-state divertor phase of the pulse (10–18.5 s), Z_{eff} from the VB measurement agrees with the Z_4 and Z_8 ratios (which is effectively Z_{eff} in this minor radius region) derived from the two continua measurements [Fig. 8(b)]. Emission from the 4 and 8 keV, being dependent on electron temperature, arises from slightly different locations in the plasma cross section [Fig. 8(c)]. It should be noted that the VB emission also covers a much larger plasma cross section than the two x-ray emissions.

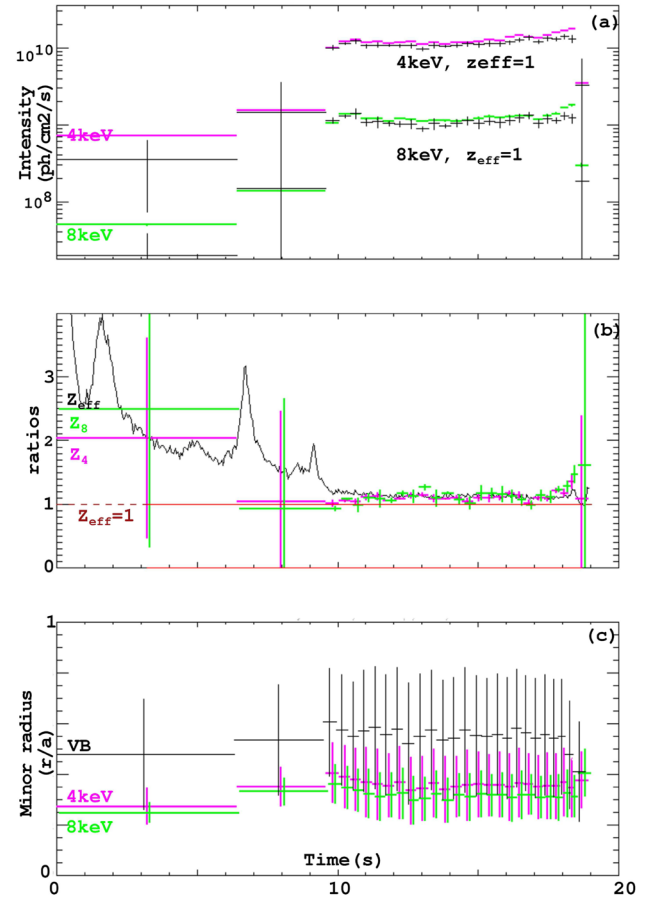


FIG. 8. (a) Si diffractor intensity measurements at the 4/8 keV (photon energy) background for JET pulse No. 96 897 and the calculated $Z_{\text{eff}} = 1$ bremsstrahlung for the same LOS. (b) Z_4 and Z_8 are the ratios of the measured and calculated 4/8 keV intensities, respectively, and here can be effectively considered as equivalent to Z_{eff} . Also shown in (b) is Z_{eff} from VB. (c) The extent of VB, 4 and 8 keV bremsstrahlung emissivities over r/a : mean with a single standard deviation error bar.

The effective peak and standard deviation of the measurements shown in Fig. 8(c) are calculated following the approach outlined in Ref. 24 for the case of line emission. Here, the continua emissivities analogously are calculated for free-free and free-bound radiation for each impurity and ion state, using flux-surface localized electron density and temperature, as a function of effective minor radius, $\langle \rho \rangle$, and standard deviation $\sigma(\rho)$,

$$\langle \rho \rangle = \rho_1 / \rho_0 \quad \text{and} \quad \sigma(\rho) = \sqrt{\rho_2 / \rho_0 - \langle \rho \rangle^2} \quad (2)$$

for $n \in \{0, 1, 2\}$, and ρ_n are defined as

$$\rho_n = \frac{1}{2\pi} \int_{R_0}^{R_{\text{wall}}} \rho^n f(Z_i; R) n_e^2(R) \epsilon(Z_{i,\text{cont}}; R) R dR, \quad (3)$$

where n_e is the density, $\epsilon(Z_{i,\text{cont}}; R)$ is the emissivity of the free-free and free-bound continua for ion species Z at an ion charge state i

integrated for all impurities and the background ion across the major radius, R . The fractional abundance, $f(Z_i; R)$, is calculated assuming coronal equilibrium. The integral limits are from the magnetic axis, R_0 , to the last closed flux-surface, R_{wall} .

Due to spatial considerations, the lower end of the line-of-sight coverage is above $r/a \sim 0.2$ because the magnetic axis of a JET plasma is above the geometric machine axis since the installation of the divertor,²⁵ and the x-ray spectrometer remains at its original position viewing the geometric center.

The agreement between the calculated “synthetic” bremsstrahlung from the two diffraction orders and the VB emission for plasmas essentially free of impurities confirms the method for evaluating the diagnostic component throughput.

Helium plasmas

For JET plasmas with helium as the majority species, the effective charge is very close to 2,²⁶ which can be used as another

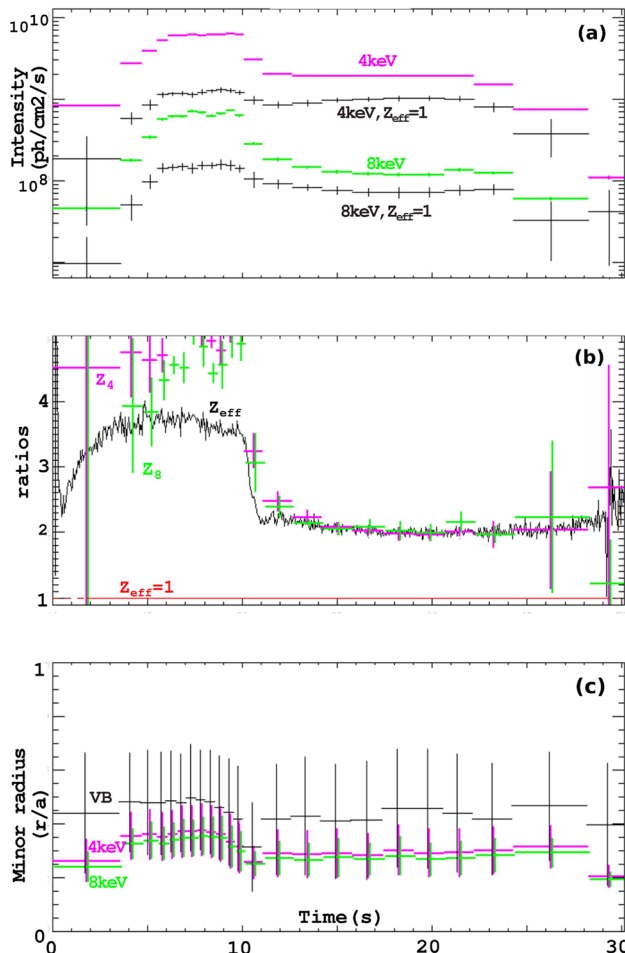


FIG. 9. (a) Si diffractor intensity levels at the 4/8 keV energies and the $Z_{eff} = 1$ calculated intensities (JET No. 97275), (b) VB Z_{eff} compared with the 4/8 keV intensity ratios, and (c) radial mean and standard deviation of the VB and 4/8 keV energies for a helium plasma.

self-calibration method. Figure 9 is the same as Fig. 8 for a $Z_{eff} = 2$ plasma. Again, good agreement between the two Z_4/Z_8 and the VB measurements provides further confirmation of the calibration of the x-ray based diagnostic, where the temporal evolution of the plasma shape, density, and temperature are different. Note that the emission from helium is dominated by free-free bremsstrahlung with little free-bound emission contribution at either the 4 keV or 8 keV x-ray energies. Here, VB, Z_4 , and Z_8 are equivalent to Z_{eff} , although they represent a different spatial extent of the respective emissivities.

Argon seeded plasmas

In large tokamaks such as JET, non-intrinsic impurities are used to seed plasmas in order to reduce the power load on the divertor and plasma facing components.²⁷ Generally speaking, in plasmas, there will also be intrinsic impurities such as beryllium, nickel (from Inconel in the JET vessel), and tungsten contingent upon the interaction of the plasma and vessel components. All of these will contribute to the continuum spectrum via free-free and free-bound channels. Figure 10 shows these emissivities over the 0.5–10 keV photon energy range at an electron temperature of 2 keV for a set of impurities with the quoted concentrations.

The fractional abundance of the ions of each element is that of equilibrium balance with the atomic data, bremsstrahlung, and free-bound recombination taken from ADAS.

The concentration of argon in seeded plasmas is significant, and the continuum emission at 4 keV from it will contribute to the total emission in these plasmas. It is reasonable to assume that the principal contributors, nickel, argon, and hydrogen ions, contribute to the 4 keV continuum. Other intrinsic impurity concentrations are not

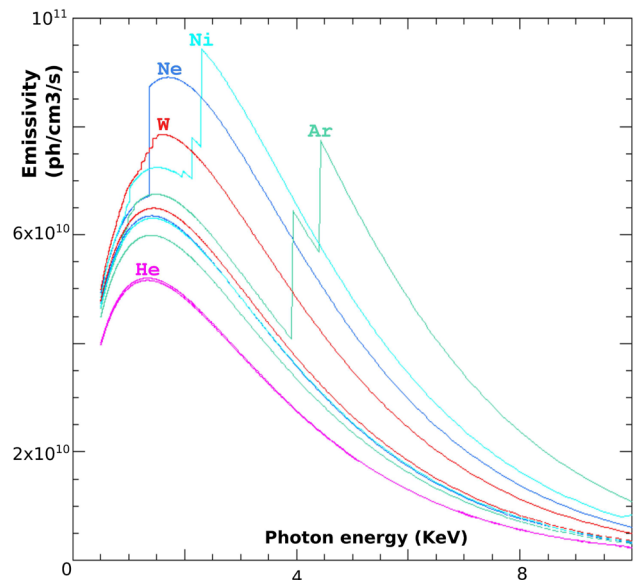


FIG. 10. Free-bound + free-free (upper curves) and free-free emissivities at 2 keV electron temperature for principal intrinsic (5%He, 0.03%Ni, 0.015%W) and extrinsic (0.2%Ne, 0.05%Ar) JET impurities.

important, judging from the spectral information available, and will not be taken into account here.

The nickel concentrations are measured and are used to calculate their component contribution to the continuum at 4 keV, assuming a constant spatial concentration profile. For each impurity, the coronal equilibrium model calculates component ion states along flux surfaces and uses local temperature and density.

Measured chord-integrated intensity I_4 at the 4 keV continua may be separated into principal ion continua as

$$I_4 = I_{Ar}C_{Ar} + I_{Ni}C_{Ni} + I_H(1 - Z_{Ni}C_{Ni} - Z_{Ar}C_{Ar}), \quad (4)$$

where the chord-integrated argon, nickel, and hydrogenic intensities (at 4 keV energy), concentrations, and mean charge are $\{I_{Ar}, I_{Ni},$

$I_H\}$, $\{C_{Ar}, C_{Ni}, C_H\}$, and $\{Z_{Ar}, Z_{Ni}, 1\}$, respectively. These quantities are calculated along the spectrometer's line of sight from emissivities evaluated at flux-surfaces. Solving for C_{Ar} ,

$$C_{Ar} = \frac{I_4 - I_{Ni}C_{Ni}I_H(Z_{Ni}C_{Ni} - 1)}{I_{Ar} - I_HZ_{Ar}}. \quad (5)$$

Chord-integrated argon concentration, C_{Ar} , can thus be calculated. Again, we emphasize this is a maximum figure, as we are assuming that the only contributors to the measured continua are from argon, nickel, and hydrogen ions.

Furthermore, a coronal balance, neglecting the effect of impurity transport, is appropriate since the peak of the x-ray emission originates closer to the core than the edge [see Figs. 8(c) and 9(c)], where transport effects are lower.²⁸

An argon seeded pulse is shown in Fig. 11. Here, we show the measured chord-integrated continua [Fig. 11(a)] along with the calculated hydrogenic continua ($Z_{eff} = 1$) at both 4 and 8 keV energies. The 8 keV component will not be analyzed further here.

In Fig. 11(b), we show measured nickel concentrations and Z_{eff} along with the argon-injection valve voltage profile. The argon concentration is from measurements in Eq. (5). $Z_{eff}(D + Ar)$ is calculated assuming this argon concentration and hydrogen only—this is for illustrative purposes, as these values should not be less than unity and should follow the argon injection profile.

As mentioned, the argon and nickel ions are principal contributors to Z_{eff} for the pulse shown here. It tracks the VB value closely, and the Ar concentration temporal profile lags the injection waveform from the piezo-valve, as expected, due to the gas-feed pipe-length, conductance, etc.

From the X-point formation at 6.3 s, the plasma- Z_{eff} calculated from D/Ar/Ni continua tracks Z_{eff} from VB rather well. Small differences in the Z_{eff} from VB and that due to nickel, argon, and the main ion may be due to (i) other impurities such as Be and W and/or (ii) due to the spatial coverage difference of the radiation indicated in Fig. 11(c) and, of course, assumptions such as constant spatial impurity profiles.

Summary

The spectrometer throughput of the JET x-ray spectrometer has been characterized at two narrow spectral bandpasses at 4 and 8 keV photon energies. Here, the plasma emission consists of free-free and free-bound continuum emission from fuel and impurity components of the plasma. Plasma- Z_{eff} is derived from these continua for a “clean” and from a He-ion majority plasma and has been derived and agrees with chord-integrated Z_{eff} based on VB measurements at the JET geometric equator.

Furthermore, we propose that the intensity for 4/8 keV photons can be used to diagnose concentrations of an externally introduced single impurity. The case highlighted here, an argon-seeded plasma, estimates of the upper-limits to the concentration, and contribution to Z_{eff} show good, although delayed, correlation with the introduced gas volume and with plasma- Z_{eff} .

Further work is envisaged to improve the analysis method for other impurity species introduced once or multiple impurities multiple times in a sequential manner into JET plasmas.

To conclude, an x-ray spectrometer that is sufficiently well aligned using visible lasers and with measured response and

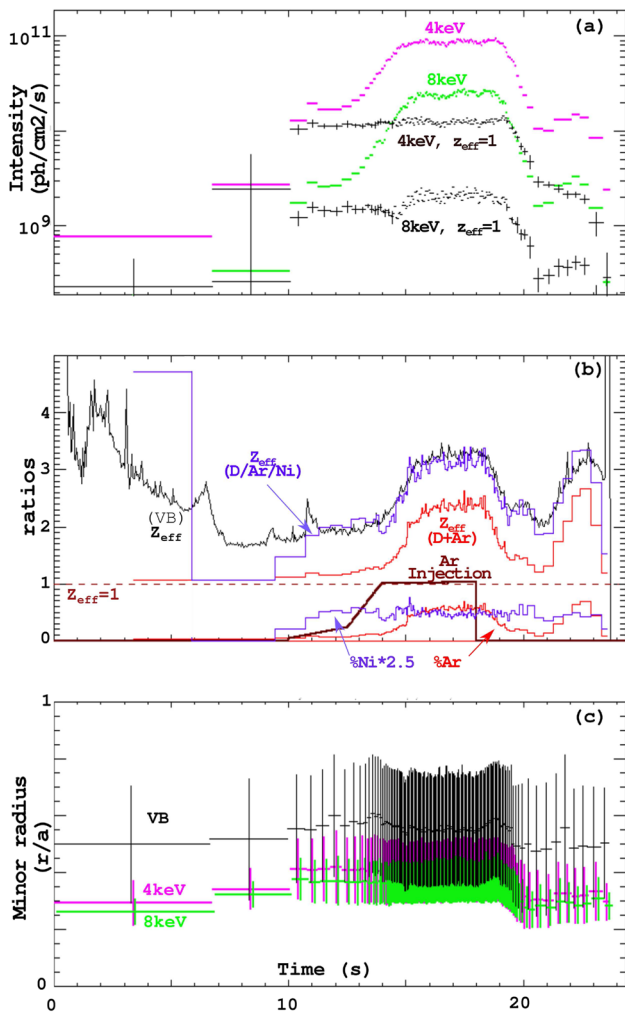


FIG. 11. Details of the argon-seeded plasma pulse (JET No. 102 598). (a) Measured and calculated intensities at 4/8 keV energies. (b) Ar gas injection waveform (brown, normalized); %Ar concentration derived from Eq. (5); Z_{eff} (red) from %Ar and hydrogenic ions; and Z_{eff} (purple) from nickel, argon, and hydrogenic ions. Ni concentrations reach $\sim 0.02\%$ and are measured by the Ge220 spectrometer. (c) Spatial emissivities assuming coronal equilibrium.

throughput of all spectrometer components is key to quantitatively interpreting the whole of the collected data across the spectrum. Be it Doppler-broadened line emission or, as demonstrated here, the continuum. In reactor-class tokamaks, x-ray diagnostic-access will be limited as diffractors can be damaged, e.g., by intense neutron bombardment. This can be mitigated by the use of neutron-hardened pre-dispersers that deflect x-ray wavelengths of interest to spectrometers: the continuum component of the spectrum may be an invaluable source of information, as shown here.

ACKNOWLEDGMENTS

The authors would like to thank S. G. Tyrrell for the technical contributions and Dr. J. Mailloux for the useful JET physics, the DTE2/3 campaign, and the reactor-relevant diagnostics discussions.

JET, which was previously a European facility, is now a UK facility collectively used by all European fusion laboratories under the EUROfusion consortium. It is operated by the United Kingdom Atomic Energy Authority, supported by DESNZ and its European partners.

This work, which has been carried out within the framework of the Contract for the Operation of the JET Facilities up to 31 October 2021, has been funded by the Euratom Research and Training Program. Since 31 October 2021, UKAEA has continued to work with the EUROfusion Consortium as an Associated Partner of Max-Planck-Gesellschaft zur Förderung der Wissenschaft e.V., represented by Max-Planck-Institut für Plasmaphysik ("IPP") pursuant to Article 9.1 of the EUROfusion Grant Agreement for Project No. 101052200. The views and opinions expressed herein do not necessarily reflect those of the European Commission.

AUTHOR DECLARATIONS

Conflict of Interest

The authors have no conflicts to disclose.

Author Contributions

A. M. Patel: Conceptualization (lead); Data curation (lead); Formal analysis (lead); Funding acquisition (supporting); Investigation (lead); Methodology (lead); Project administration (supporting); Resources (equal); Software (lead); Supervision (lead); Validation (lead); Visualization (lead); Writing – original draft (lead); Writing – review & editing (equal). **N. C. Hawkes:** Investigation (supporting); Writing – review & editing (supporting). **K.-D. Zastrow:** Formal analysis (supporting); Funding acquisition (supporting); Investigation (supporting); Methodology (supporting); Project administration (supporting); Resources (supporting); Software (supporting); Supervision (supporting); Validation (supporting); Writing – review & editing (supporting). **M. O'Mullane:** Conceptualization (equal); Data curation (supporting); Formal analysis (supporting); Investigation (supporting); Methodology (supporting); Software (supporting); Writing – review & editing (equal).

DATA AVAILABILITY

To obtain further information on the data and models underlying this paper, please contact PublicationsManager@ukaea.uk.

REFERENCES

- ¹P. H. Rebut and B. E. Keen, "The JET experiment: Evolution, present status, and prospects," *Fusion Technol.* **11**(1), 13–42 (1987).
- ²C. F. Maggi *et al.*, "Overview of T and D-T results in JET with ITER-like wall," *Nucl. Fusion* **64**, 112012 (2023).
- ³V. K. Zotta, L. Garzotti, S. Gabriellini, R. Gatto, C. Bourdelle, C. Giroud, L. Frassinetti, D. Frigione, D. B. King, D. L. Keeling *et al.*, "Predictive modelling of JET baseline scenarios from DTE2 towards DTE3," in 50th EPS Conference on Plasma Physics Salamanca, 8–12 July 2024.
- ⁴M. Bitter, S. Von Goeler, S. Cohen, K. W. Hill, S. Sesnic, F. Tenney, J. Timberlake, U. I. Safronova, L. A. Vainshtein, J. Dubau *et al.*, "Dielectronic satellite spectra of hydrogenlike titanium (Ti XXII)," *Phys. Rev. A* **29**(2), 661 (1984).
- ⁵TFR Group, J. Dubau, and M. Loulergue, "High-resolution spectra from inner-shell transitions in highly ionised chromium (Cr XIX–XXIII)," *J. Phys. B: At., Mol. Opt. Phys.* **15**(7), 1007 (1982).
- ⁶J. Dubau and S. Volonte, "Dielectronic recombination and its applications in astronomy," *Rep. Prog. Phys.* **43**(2), 199 (1980).
- ⁷R. Bartiromo, F. Bombarda, R. Giannella, S. Mantovani, L. Panaccione, and G. Pizzicaroli, "JET high resolution bent crystal spectrometer," *Rev. Sci. Instrum.* **60**(2), 237–243 (1989).
- ⁸H. H. Johann, "Die Erzeugung Lichtstarker Röntgenspektren mit Hilfe von Konkavkristallen," *Z. Phys.* **69**, 185–206 (1931).
- ⁹B. Kos, T. Vasilopoulou, S. W. Mosher, I. A. Kodeli, R. E. Grove, J. Naish, B. Obyrk, R. Villari, and P. Batistoni, "Analysis of DD, TT and DT neutron streaming experiments with the ADVANTG code," *EPJ Web Conf.* **225**, 02003 (2020).
- ¹⁰N. A. Pablant, Z. Cheng, M. O'Mullane, L. Gao, R. Barnsley, M. N. Bartlett, M. Bitter, E. Bourcart, G. V. Brown, M. De Bock *et al.*, "Results from a synthetic model of the ITER XPCS-Core diagnostic based on high-fidelity x-ray ray tracing," *Rev. Sci. Instrum.* **95**(8), 083517 (2024).
- ¹¹A. E. Shumack, J. Rzakiewicz, M. Chernyshova, K. Jakubowska, M. Scholz, A. Byszuk, R. Cieszkowski, T. Czarski, W. Dominik, L. Karpinski *et al.*, "X-ray crystal spectrometer upgrade for ITER-like wall experiments at JET," *Rev. Sci. Instrum.* **85**(11), 11E425 (2014).
- ¹²D. J. Campbell, A. Loarte, D. Boilson, X. Bonnin, P. de Vries, L. Giancarli, Y. Gribov, M. Henderson, S. H. Kim, P. Lamalle *et al.*, "ITER research plan within the staged approach (level III—Final version)," ITER Technical Report No. ITR-24-005, 2024.
- ¹³M. Z. Tokar, "An assessment for the erosion rate of demo first wall," *Nucl. Fusion* **58**(1), 016016 (2017).
- ¹⁴M. Z. Tokar, "Assessment for erosion of and impurity deposition on first mirrors in a fusion reactor," *Nucl. Fusion* **58**(9), 096007 (2018).
- ¹⁵W. Biel, M. Ariola, I. Bolshakova, K. J. Brunner, M. Ceconello, I. Duran, Th. Franke, L. Giacomelli, L. Giannone, F. Janky, A. Krimmer, R. Luís, A. Malaquias, G. Marchiori, O. Marchuk, D. Mazon, A. Pironti, A. Quercia, N. Rispoli, S. E. Shawish *et al.*, "Development of a concept and basis for the DEMO diagnostic and control system," *Fusion Eng. Des.* **179**, 113122 (2022).
- ¹⁶R. Bartiromo, R. Giannella, M. L. Apicella, F. Bombarda, S. Mantovani, and G. Pizzicaroli, "Time resolving bent crystal spectrometer for tokamak plasma diagnostics," *Nucl. Instrum. Methods Phys. Res.* **225**(2), 378–384 (1984).
- ¹⁷C. Nicholas, H. Summers, and M. O'Mullane, https://www.adas.ac.uk/adaseu_site/reports/publ_2.pdf, 2010.
- ¹⁸F. Bombarda, R. Giannella, E. Källne, G. J. Tallents, F. Bely-Dubau, P. Faucher, M. Cornille, J. Dubau, and A. H. Gabriel, "Observations and comparisons with theory of the heliumlike and hydrogenlike resonance lines and satellites of nickel from the JET tokamak," *Phys. Rev. A* **37**(2), 504 (1988).
- ¹⁹J. Rzakiewicz, W. Dominik, M. Scholz, K. D. Zastrow, M. Chernyshova, T. Czarski, H. Czyrkowski, R. Dabrowski, K. Jakubowska, L. Karpinski *et al.*, "Novel design of triple GEM detectors for high-resolution x-ray diagnostics on JET," Technical Report No. EFDA-JET-CP(11)07/02, 2011.
- ²⁰J. E. Rice, F. Sciortino, M. Gu, N. Cao, J. W. Hughes, J. H. Irby, E. S. Marmar, S. Mordijck, M. L. Reinke, and R. Reksoatmodjo, "The very high n Rydberg series of Ar¹⁶⁺ in Alcator C-mod tokamak plasmas," *J. Phys. B: At., Mol. Opt. Phys.* **54**(17), 175701 (2021).
- ²¹A. Burgess and H. P. Summers, "Radiative gaunt factors," *Mon. Not. R. Astron. Soc.* **226**(2), 257–272 (1987).

- ²²M. Brix, N. C. Hawkes, A. Boboc, V. Drozdov, S. E. Sharapov, and JET-EFDA Contributors, "Accuracy of EFIT equilibrium reconstruction with internal diagnostic information at JET," *Rev. Sci. Instrum.* **79**(10), 10F325 (2008).
- ²³H. Meister, R. Fischer, L. D. Horton, C. F. Maggi, D. Nishijima, C. Giroud, K.-D. Zastrow, B. Zaniol, and JET-EFDA Contributors, " Z_{eff} from spectroscopic bremsstrahlung measurements at ASDEX Upgrade and JET," *Rev. Sci. Instrum.* **75**(10), 4097–4099 (2004).
- ²⁴L. G. Eriksson, E. Righi, and K. D. Zastrow, "Toroidal rotation in ICRF-heated H-modes on JET," *Plasma Phys. Controlled Fusion* **39**(1), 27 (1997).
- ²⁵E. Bertolini, "JET with a pumped divertor: Design, construction, commissioning and first operation," *Fusion Eng. Des.* **30**(1–2), 53–66 (1995).
- ²⁶A. Huber, S. Brezinsek, V. Huber, E. R. Solano, G. Sergienko, I. Borodkina, S. Aleiferis, A. Meigs, D. Tskhakaya, M. Sertoli, M. Baruzzo, D. Borodin, P. Carvalho, E. Delabie, D. Douai, A. Kirschner, K. Lawson, Ch. Linsmeier, J. Mailloux, S. Menmuir, Ph. Mertens, E. Pawelec, J. Romazanov, A. Shaw, and JET Contributors, "Understanding tungsten erosion during inter/intra-ELM periods in He-dominated JET-ILW plasmas," *Phys. Scr.* **96**(12), 124046 (2021).
- ²⁷G. F. Matthews, B. Balet, J. G. Cordey, S. J. Davies, G. M. Fishpool, H. Y. Guo, L. D. Horton, M. G. v. Hellermann, L. C. Ingesson, J. Lingertat *et al.*, "Studies in JET divertors of varied geometry. II: Impurity seeded plasmas," *Nucl. Fusion* **39**(1), 19 (1999).
- ²⁸C. Giroud, R. Barnsley, P. Buratti, I. H. Coffey, M. v. Hellermann, C. Jupén, K. D. Lawson, A. Meigs, M. O'Mullane, A. D. Whiteford, K.-D. Zastrow, and JET EFDA Contributors, "Method for experimental determination of Z dependence of impurity transport on JET," *Nucl. Fusion* **47**(4), 313 (2007).
- ²⁹H. P. Summers, The ADAS User Manual, version 2.6, <http://www.adas.ac.uk>, 2004.